remote sensing

MDPI

Article

Change Detection from SAR Images Based on Convolutional Neural Networks Guided by Saliency Enhancement

Liangliang Li [1], Hongbing Ma [1,*] and Zhenhong Jia [2]

[1] Department of Electronic Engineering, Tsinghua University, Beijing 100084, China; leeliangliang@tsinghua.edu.cn
[2] College of Information Science and Engineering, Xinjiang University, Urumqi 830046, China; jzhh@xju.edu.cn
* Correspondence: hbma@tsinghua.edu.cn

Abstract: Change detection is an important task in identifying land cover change in different periods. In synthetic aperture radar (SAR) images, the inherent speckle noise leads to false changed points, and this affects the performance of change detection. To improve the accuracy of change detection, a novel automatic SAR image change detection algorithm based on saliency detection and convolutional-wavelet neural networks is proposed. The log-ratio operator is adopted to generate the difference image, and the speckle reducing anisotropic diffusion is used to enhance the original multitemporal SAR images and the difference image. To reduce the influence of speckle noise, the salient area that probably belongs to the changed object is obtained from the difference image. The saliency analysis step can remove small noise regions by thresholding the saliency map, and interest regions can be preserved. Then an enhanced difference image is generated by combing the binarized saliency map and two input images. A hierarchical fuzzy c-means model is applied to the enhanced difference image to classify pixels into the changed, unchanged, and intermediate regions. The convolutional-wavelet neural networks are used to generate the final change map. Experimental results on five SAR data sets indicated the proposed approach provided good performance in change detection compared to state-of-the-art relative techniques, and the values of the metrics computed by the proposed method caused significant improvement.

Keywords: synthetic aperture radar image; change detection; saliency detection; convolutional-wavelet neural networks; hierarchical fuzzy c-means

Citation: Li, L.; Ma, H.; Jia, Z. Change Detection from SAR Images Based on Convolutional Neural Networks Guided by Saliency Enhancement. *Remote Sens.* **2021**, *13*, 3697. https://doi.org/10.3390/rs13183697

Academic Editors: Kuo-Chin Fan, Yang-Lang Chang, Toshifumi Moriyama and Ying-Nong Chen

Received: 12 July 2021
Accepted: 8 September 2021
Published: 16 September 2021

1. Introduction

The synthetic aperture radar (SAR) imaging process is not affected by sunlight, clouds, or the atmosphere because of the microwave imaging principle. In the field of SAR image processing, change detection is a very important topic. SAR images are an important information resource for change detection when studying disaster relief, agricultural detection, and urban planning, especially when evaluating the damage caused by natural disasters [1–4]. Because of the interference of scattering echo, speckle noise will inevitably be generated; it has the nature of multiplicative noise, and it seriously affects the interpretation of SAR images [5]. Therefore, noise suppression is an important task in the process of change detection. In recent decades, many change detection methods utilizing SAR imagery have been introduced, and these approaches can be divided into two categories: coherent and incoherent change detection methods, depending on whether interferometric phase information is used. In this paper, we mainly discuss incoherent change detection methods [6].

In terms of incoherent SAR image change detection algorithms, supervised and unsupervised methods are the most used. The main problem associated with supervised methods is the lack of ground reference data, which often involves manual marking processes that are labor-intensive and time-consuming. Unsupervised SAR change detection

generally includes three basic steps: speckle noise reduction, difference map generation, and classification [7].

There are problems that influence the effect of SAR image change detection. First, the inherent speckle noise in the SAR images may cause false positives. If we use the denoising method directly, we can also remove useful information in the denoising process. Second, the difference image (DI) influences the detection results, and the changed information may be lost when obtaining the DI. Finally, because the prior information is used in the supervised models to train the classifier, the supervised models may generate a performance superior to the unsupervised models. Nevertheless, prior information is usually achieved by manual annotation, which requires much work and affects the generalization of the model. Hence, in terms of the SAR image change detection, effective denoising, feature extraction, and prior information acquisition ought to be considered.

As the result of these findings, for the sake of suppressing the speckle noise and preserving interest information, one saliency detection method is used to extract the interesting regions that probably pertain to the changed objects. To extract the changed information, the convolutional-wavelet neural networks (CWNNs) model is utilized to learn features from the denoised images and the difference image. The speckle reducing anisotropic diffusion (SRAD) is used to enhance the input images and the difference image. The saliency detection is performed on the enhanced difference image, and the interest regions are extracted. The hierarchical fuzzy c-means clustering (HFCM) model is used for pre-classification. Finally, the CWNN model is used to generate the final change map. Experiments on qualitative and quantitative comparisons demonstrate the advantages and innovations of the proposed SAR image change detection algorithm. The major contributions of the proposed method are concluded as follows.

(1) A saliency detection model is used in the proposed method, which aims to generate the salient regions that probably belong to the changed objects. The saliency detection model can extract attractive and compact salient areas from the difference image with a simple operation. It can remove background pixels and suppress noise.
(2) A hierarchical fuzzy c-means clustering (HFCM) model is introduced in the proposed method and is used to select pixels with high probability of becoming changed or unchanged. The samples from the changed and unchanged parts are selected as the training set for the convolutional neural network.
(3) A convolutional neural network based on dual-tree complex wavelet transform is constructed that aims to enhance the accuracy of change detection.

2. Related Works

2.1. SAR Image Preprocessing

To cope with the speckle noise in SAR images, many noise reduction algorithms have been proposed in the past few years. The classical methods are probabilistic-patch-based (PPB) filter [8], speckle reducing anisotropic diffusion (SRAD) [9], non-local means filter [10,11], total variation model [12], block-matching 3D filtering [13], deep multi-scale recurrent network [14], multilook and refined Lee filtering [15], etc. Zheng et al. [16] introduced a SAR change detection method based on PPB filter and k-means clustering model where the PPB filter is used to suppress the speckle noise, and the two difference images are generated by subtraction and log-ratio operators, respectively; then the k-means clustering model is performed on the combined difference image to obtain the final change map. Because of the high computational complexity of the PPB algorithm, the whole change detection algorithm is relatively time-consuming. Su et al. [17] proposed a SAR change detection technique via non-local means with ratio similarity measurement; the enhanced non-local means model plays a role in suppressing speckle noise. Some other denoising algorithms have also generated good results in remote sensing image change detection. Lou et al. [18] introduced the ROF model semi-implicit denoising method for speckle reduction into the SAR change detection process, and this denoising algorithm played an important role in improving the accuracy of change detection. Wang et al. [19]

proposed a new change detection technique based on logarithmic transformation and a total variation denoising approach. Liu et al. [20] introduced a change detection method based on mathematical morphology and a k-means clustering model, and the accuracy of the change detection improved. The nonsubsampled contourlet transform (NSCT) and nonsubsampled shearlet transform (NSST) are widely used in image fusion and denoising [21–27]. Chen et al. [28] introduced the NSCT-hidden Markov tree (NSCT-HMT) model to the remote sensing image change detection; Li et al. [29] proposed a multitemporal remote sensing image change detection algorithm based on the NSCT denoising model. Zhou et al. [30] introduced the image denoising model via NSST for SAR change detection; Shen et al. [31] proposed an image change detection approach using a Kalman filter and nonlocal means filter in the NSST domain. Because the different decomposition layers of NSCT and NSST have a certain impact on the image denoising effect, finding the appropriate decomposition layer is also an important problem. As an important part of SAR image processing, the denoising model is very important in the pre-processing of change detection.

2.2. DI Generation

The commonly used methods for generating the difference image (DI) are the subtraction operator and the ratio operator. Because the model of speckle noise inherent in SAR images is multiplicative random noise [5], the subtraction operator cannot suppress speckle-noise effectively. Compared with the subtraction operator, the ratio operator is the division between two SAR images. It can overcome the disadvantage of sensitivity to multiplicative noise. Based on the ratio operator, some improved models such as the log-ratio operator, mean-ratio operator, and neighborhood-based ratio operator are utilized. The log-ratio operator is robust to calibration and radiometric errors [32], it can reduce the influence of speckle noise, and it is widely used to generate the difference image, but the noisy regions can still be seen in the difference image. To create a different image with rich information, a combination of different operators has been widely used in recently published articles. Hou et al. [32] introduced the Gauss-log ratio operator as an improvement of the log-ratio operator, and this change detection method combines the difference images obtained by Gauss-log ratio and log-ratio operators in the discrete wavelet transform domain to generate a fused difference image. Zhang et al. [33] introduced the SAR change detection approach via fusing the Gauss-log ratio and subtraction operation in the shearlet transform domain. In the references [34,35], the difference images generated by mean-ratio and log-ratio operators, respectively, are effectively fused in a wavelet domain.

In recent years, some scholars have been working to obtain a difference map with more regions of interest and noise suppression, and the saliency detection was introduced. The saliency detection model can extract attractive and compact salient regions from the difference image with a simple operation [36]. It can remove the background pixels and reduce the influence of speckle noise. Geng et al. [36] introduced saliency-guided deep neural networks for SAR change detection. Zheng et al. [37] proposed an unsupervised saliency-guided SAR image change detection method where the context-aware saliency detection model is used to compute the difference image of the log-ratio operator. The thresholding model then combines the original SAR images to generate the new difference image; finally, the principal component analysis (PCA) and k-means clustering models are used to create the change map. This method offers a better performance in remote sensing image change detection compared to other state-of-the-art algorithms without saliency detection. Wang et al. [38] used the pattern and intensity distinctive analysis model to generate the saliency map of the difference image. Majidi et al. [39] proposed a saliency-guided neighborhood ratio model for automatic change detection. Li et al. [40] introduced an unsupervised SAR image change detection algorithm combining PCANet with saliency detection, and the accuracy of change detection was significantly improved.

2.3. Application of Classification to Change Detection

For the classification step of SAR image change detection, the pixels in the difference image are usually classified into changed and unchanged areas. These classification methods can be divided into unsupervised and supervised models. In terms of unsupervised change detection, the thresholding-, active contours-, and clustering-based methods are widely utilized in the classical change detection algorithms, and the prior information of the training set is not needed. Moser et al. [41] utilized generalized minimum-error thresholding for unsupervised SAR image change detection. Celik et al. [42] used a region-based active contour model for change detection. Hao et al. [43] used a superpixel-based active contour model for SAR image change detection. Meanwhile, clustering-based algorithms have been introduced for change detection. Jia et al. [44] introduced the multiple kernel k-means clustering with local-neighborhood information for remote sensing image change detection. In reference [45], the modified fuzzy c-means (FCM) algorithm was performed on the difference image to generate the change map. The FCM-based models cannot generate accurate change detection results, mainly because of the use of overall optimization objectives. Li et al. [46] introduced the fuzzy local-information c-means clustering model (FLICM) into the field of SAR change detection.

The deep learning-based classification model has had a rapid development and application in recent years, and these classification methods have generated an excellent performance and higher classification accuracy rate than the abovementioned approaches. Zhang et al. [47] proposed two-phase object-based deep learning for unsupervised SAR change detection. Gao et al. [48] introduced the channel weighting-based deep cascade network for unsupervised change detection. The PCANet was first proposed by Chan et al. [49] in 2015, and the PCANet model was introduced into the change detection field by Gao et al. [50] in 2016. This PCANet-based unsupervised change detection model achieves good performance, but it is quite time-consuming. Liu et al. [51] presented the convolutional neural network (CNN) model for unsupervised SAR change detection. Duan et al. [52] introduced a SAR image segmentation algorithm using convolutional-wavelet neural networks (CWNNs), and this technique achieves good segmentation results and suppresses the speckle noise. Gao et al. [53] introduced the CWNN model for unsupervised SAR image change detection, and it performs well in change detection.

Inspired by the SAR image change detection algorithms introduced previously, an effective and practical SAR image change detection utilizing saliency-guided convolutional neural networks is proposed in this paper.

3. Proposed SAR Image Change Detection Method

In this section, we elaborate on the proposed unsupervised SAR image change detection method. The proposed method can be divided into the following steps: difference image, extraction of salient regions, pre-classification, and classification by CWNN model. The log-ratio operator is used to generate the initial difference image, then the saliency detection is utilized to obtain the salient regions. The HFCM model is used for pre-classification. Finally, the CWNN model is used to generate the final change map. The flow chart of the proposed automatic change detection algorithm is given in Figure 1.

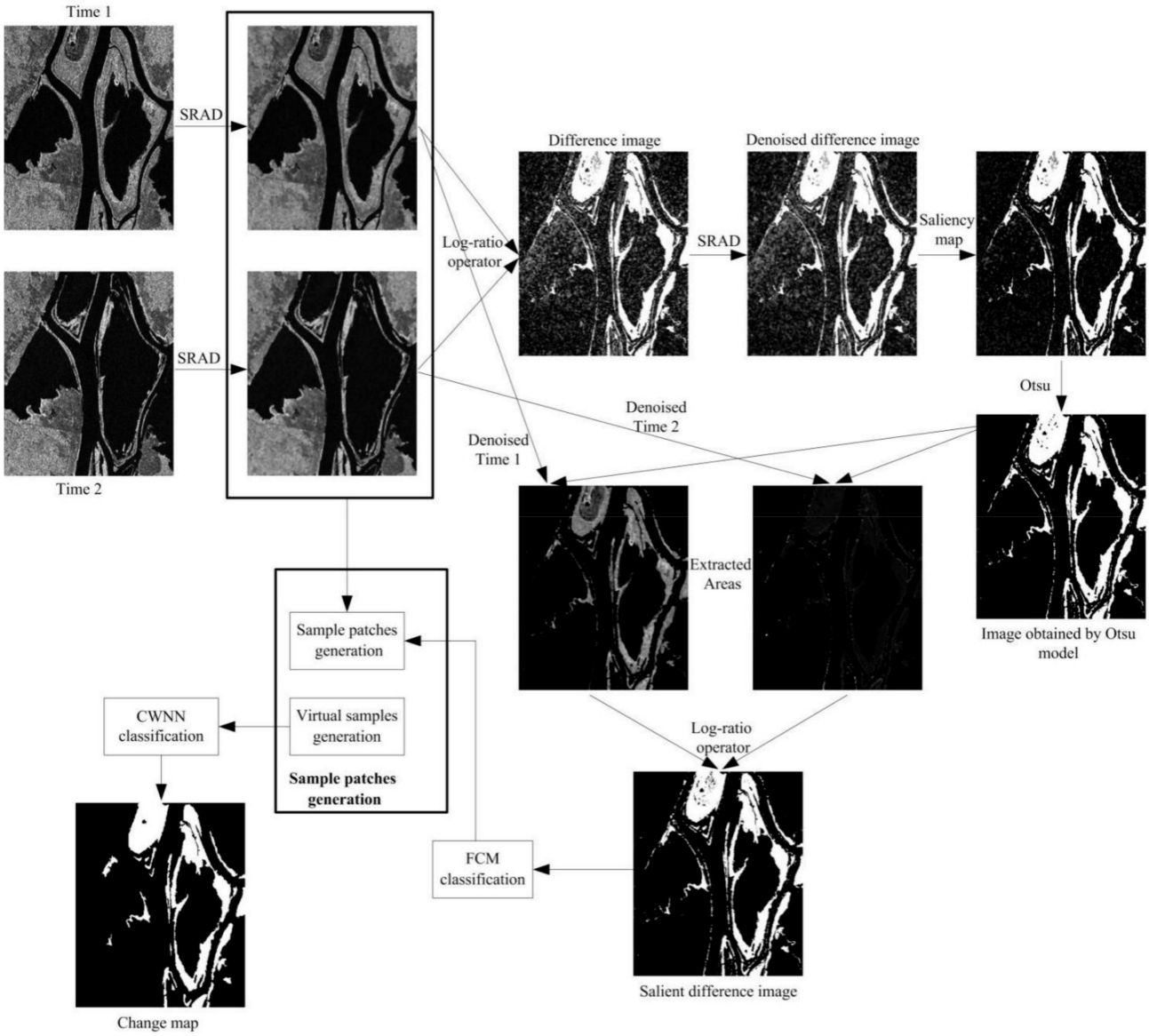

Figure 1. The flow chart of the proposed SAR image change detection model.

3.1. Difference Image Generated by Log-Ratio Operator

Given two co-registered multi-temporal SAR images I_1 and I_2, which are obtained from the same region at different times, t_1 and t_2, respectively, the purpose of SAR image change detection is to produce a difference image that reflects the change information between t_1 and t_2.

The initial SAR images will be affected by noise, and the speckle reducing anisotropic diffusion (SRAD) [9] is used to suppress the noise in multi-temporal SAR images I_1 and I_2, generating the denoised images X_1 and X_2 corresponding to I_1 and I_2, respectively. Figure 2 shows the example of the Ottawa images denoised by SRAD, and the peak signal-to-noise ratio (PSNR) index is used to measure the denoising effect; we can see that the noise is suppressed effectively from the area with the red box.

In this section, the initial difference image ($DI1$) is generated by the log-ratio (LR) operator, then SRAD is performed on the $DI1$, and the denoised difference image $DI2$ is obtained. The corresponding equation is:

$$DI1 = \left| \log \frac{X_2}{X_1} \right| = |\log X_2 - \log X_1| \tag{1}$$

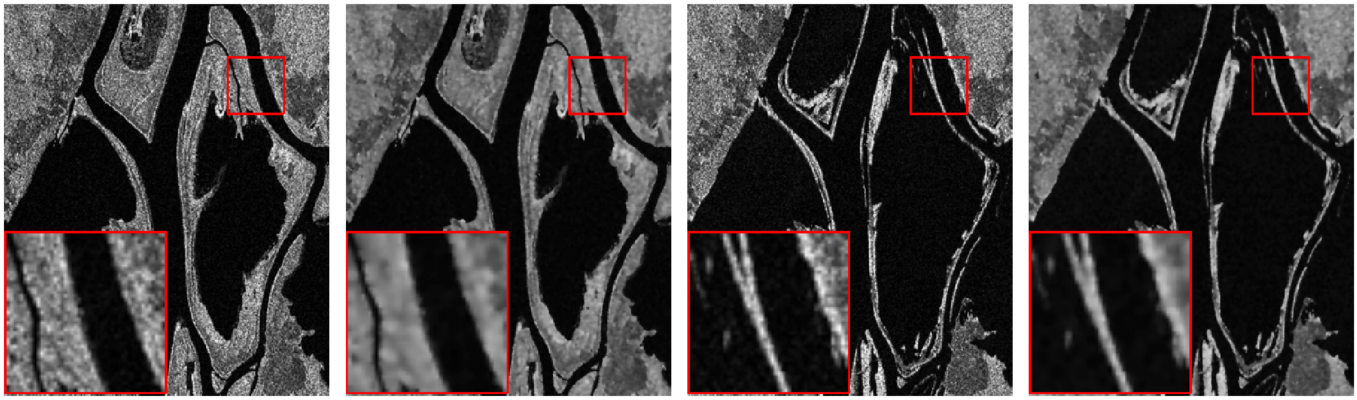

(**a**) (**b**) (**c**) (**d**)

Figure 2. The example of SRAD denoising for Ottawa images. (**a**) Time 1 of Ottawa; (**b**) denoised image of Time 1 (PSNR = 24.0372); (**c**) Time 2 of Ottawa; (**d**) denoised image of Time 2 (PSNR = 25.2647).

3.2. Extraction of Salient Regions

Visual saliency regions contain information for visual image processing. In this section, the saliency detection theory is adopted to guide the change detection of SAR images. The initial difference image has a strong contrast region, and this is the salient region. We utilize the saliency detection model to locate the similar-change areas and optimize the proposed change detection task.

Suppose the X_p denotes the intensity value of one pixel p in the image X. The saliency value $V(p)$ of the pixel p can be calculated by the following [54]:

$$V(p) = |X_p - X_1| + |X_p - X_2| + \cdots + |X_p - X_N| \tag{2}$$

where N is the total number of pixels in X. When two pixels have the same value of intensity, their saliency values are equal. Equation (2) can be modified as follows:

$$V(p) = \sum_{j=0}^{L-1} M_j |X_p - X_j| \tag{3}$$

where j depicts the pixel intensity, M_j shows the number of pixels with an intensity equal to j, and L denotes the number of gray levels.

The saliency map of the denoised difference image $DI2$ is calculated by Equations (2) and (3), and we define the saliency map as D_S.

3.3. Preclassification

In this section, the automatic threshold Otsu model is used to generate the binarized saliency map D'_s, and it is calculated by the following [40]:

$$D'_s(x,y) = \begin{cases} 1 & p(x,y) \geq \tau \\ 0 & p(x,y) \leq \tau \end{cases} \tag{4}$$

where $p(x,y)$ denotes the gray value of the pixel in the salient area D_s. The parameter τ shows the threshold computed by the Otsu model. In terms of D'_s, the value 1 indicates the salient pixels, and the value 0 indicates the non-salient pixels. The regions corresponding to the multi-temporal SAR images are extracted with the D'_s, and the following equation is given:

$$ds_i = X_i \odot D'_s \tag{5}$$

where $X_i (i = 1, 2)$ shows the matrix generated by the denoised multi-temporal SAR images. $\odot$ denotes the dot product operator.

The new salient difference image D_2 is generated by utilizing the log-ratio model, and it is calculated by the following:

$$D_2 = \left| \log \frac{ds_1 + 1}{ds_2 + 1} \right| \tag{6}$$

When the D_2 is generated, the hierarchical FCM clustering (HFCM) model [55] is used to classify the D_2 into three components: the changed class Ω_c, the unchanged class Ω_u, and the intermediate class Ω_i. The Ω_c and Ω_u are selected as the training samples, and Ω_i is further classified by CWNN. More details of the hierarchical FCM clustering are contained in reference [55].

3.4. Classification by CWNN

CWNN was developed from convolutional neural networks (CNNs); it consists of convolutional layers, max-pooling layers, and fully connected layers [52,53]. In the CWNN model, the dual-tree complex wavelet transform (DTCWT) is introduced into the CNN model to reduce the effect of speckle noise in the SAR images. DTCWT has the advantages of good direction selectivity, limited redundancy, and a good reconstruction effect. DTCWT can decompose the layer preceding the pooling layer into eight components, including two low-frequency sub-bands LL_1 and LL_2, and the high-frequency sub-bands in six orientations, $\pm 15^\circ$, $\pm 45^\circ$, and $\pm 75^\circ$ (given by LH_1, LH_2, HL_1, HL_2, HH_1, and HH_2) [56]. We chose the average of the two low-frequency sub-bands as the output of the pooling layer. Firstly, low-frequency components maintain the structures of the input layer according to the specified rules to better represent the patch of the input image. Secondly, some noises are suppressed by losing the high-frequency components.

In the CWNN method, the input of a wavelet pooling layer presents the output of the previous convolutional layer. In terms of each input feature map x, the DTCWT is utilized to generate the sub-bands:

$$\{LL_1, LL_2, LH_1, LH_2, HL_1, HL_2, HH_1, HH_2\} = f(x_i) \tag{7}$$

where $f(\cdot)$ denotes the DTCWT function. The average of the low-frequency components is adopted as the output of the wavelet pooling layer, and the corresponding formula is defined as follows:

$$LL_{mean} = \frac{1}{2}(LL_1 + LL_2) \tag{8}$$

where LL_{mean} represents the output of the wavelet pooling layer.

Figure 3 shows an example of the wavelet pooling layer. x_i denotes one feature map after the convolutional layer. The eight sub-bands are generated by the DTCWT performed on the feature map, including two low-frequency sub-bands and six high-frequency sub-bands. The output feature map is achieved by averaging the two low-frequency sub-bands.

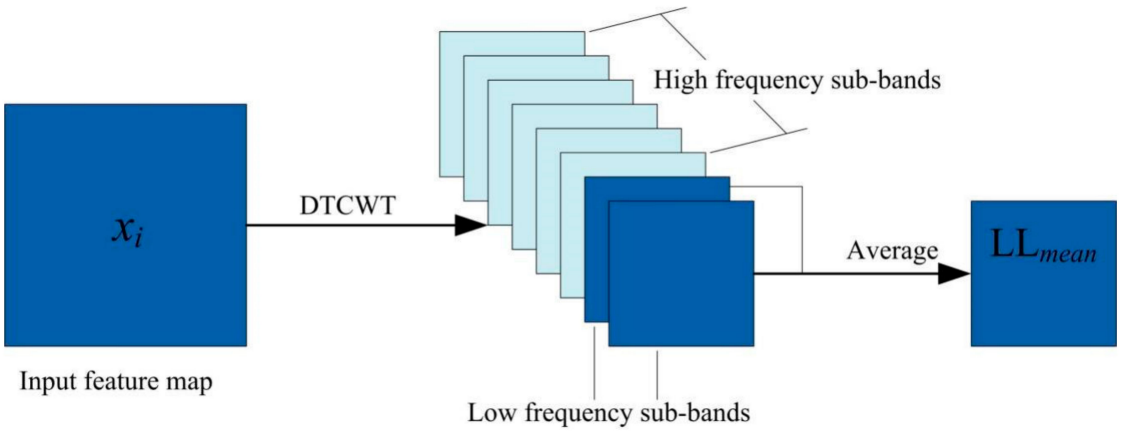

Figure 3. Wavelet pooling layer.

The structure of CWNN is depicted in Figure 4. C_2 and C_4 denote the two convolutional layers, W_3 and W_5 present the wavelet pooling layer. Hence, the network can be depicted as $\{I_1, C_2, W_3, C_4, W_5, F_6, O_7\}$. I_1 shows the input layer, and all the input image patches are resampled to 28 × 14. C_2 presents the convolutional layer with six convolutional kernels of 5 × 3. This layer generates six feature maps sized 24 × 12. W_3 shows the wavelet pooling layer. In this layer, all the input feature maps are decomposed with one-level DTCWT. This wavelet pooling layer generates six feature maps with the size of 12 × 6. C_4 depicts the convolutional layer with 12 convolutional kernels of 5 × 3. This layer produces 12 feature maps sized 8 × 4. W_5 shows the wavelet pooling layer, generating 12 feature maps sized 4 × 2. F_6 represents the fully connected layer with 96 units. O_7 presents the output layer with two units.

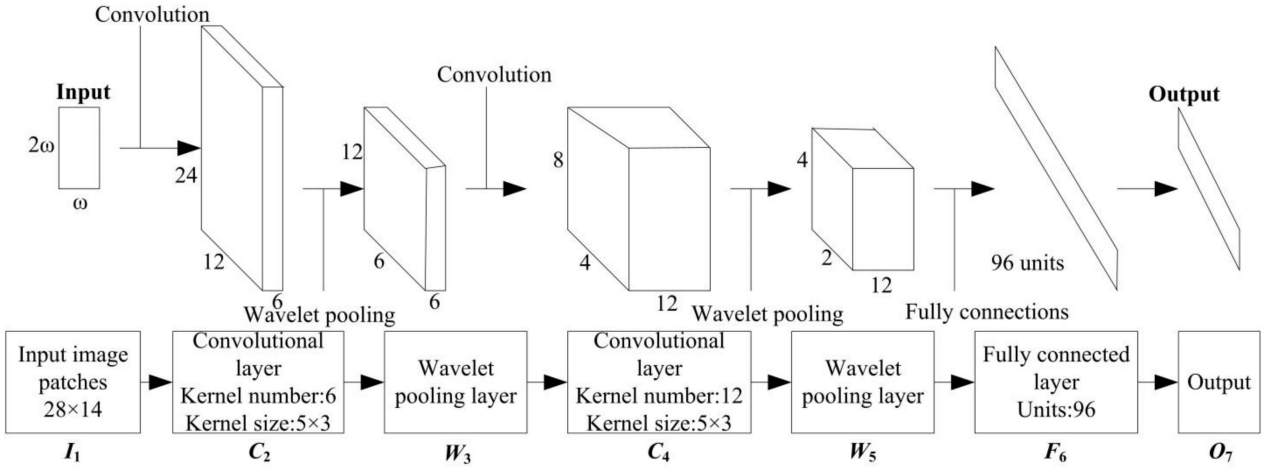

Figure 4. The structure of CWNN.

In this section, the real samples and virtual samples are used as the training samples. When the CWNN training is finished, the image patches from Ω_i are classified into changed and unchanged components, and the final change map is generated by the results of preclassification and CWNN classification.

4. Experimental Results and Discussions

4.1. Data Set Descriptions

In this section, four real SAR image data sets and one simulated SAR image data set were used to demonstrate the effectiveness of the proposed SAR image change detection method. Figures 5–9 show the SAR image data sets. Figure 5 is the Ottawa data set of two SAR images sized 290 × 350, captured by Radarsat-1, and they were acquired in May and August 1997. Figure 6 is the Coastline data set of two SAR images in Dongying, China, sized 450 × 280, captured by Radarsat-2; they were obtained in June 2008 and June 2009. Figure 7 shows the De Gaulle Airport data set of two SAR images acquired by ERS-1; they were taken in July 1997 and October 1998. The size of each SAR image is 240 × 370. Figure 8 is the Wenchuan data set of two SAR images sized 442 × 301, captured by ESA/ASAR on 3 March 2008 and 16 June 2008. These data mainly reflect the change caused by earthquake. The fifth data set in Figure 9 is the simulated data set of SAR images of the size 335 × 470 related to the village of Feltwell in the U.K. An image captured by the Daedalus 1268 Airborne Thematic Mapper (ATM) multispectral scanner was used as the reference image, and this image was assumed to be the Time 1 image of the data set. The Time 2 image was artificially generated from the reference one, and the land cover change was simulated by inserting some changes into the Time 1 image. The ground-truth images in Figures 5–9 were produced by artificial tagging with prior information. A description of the five data sets used in the experiment is given in Table 1.

Table 1. The five data sets used in the experiment.

Place	Event	Pre-Data	Post-Data	Size	Satellite	Sensor Type
Ottawa	Flood	May 1997	August 1997	290 × 350	Radarsat-1	SAR
Coastline	Flood	June 2008	June 2009	450 × 280	Radarsat-2	SAR
De Gaulle Airport	Airstrip	July 1997	October 1998	240 × 370	ERS-1	SAR
Wenchuan	Earthquake	3 March 2008	16 June 2008	442 × 301	ESA/ASAR	SAR
Village of Feltwell	Land cover variations	None	None	335 × 470	Daedalus 1268 ATM	SAR

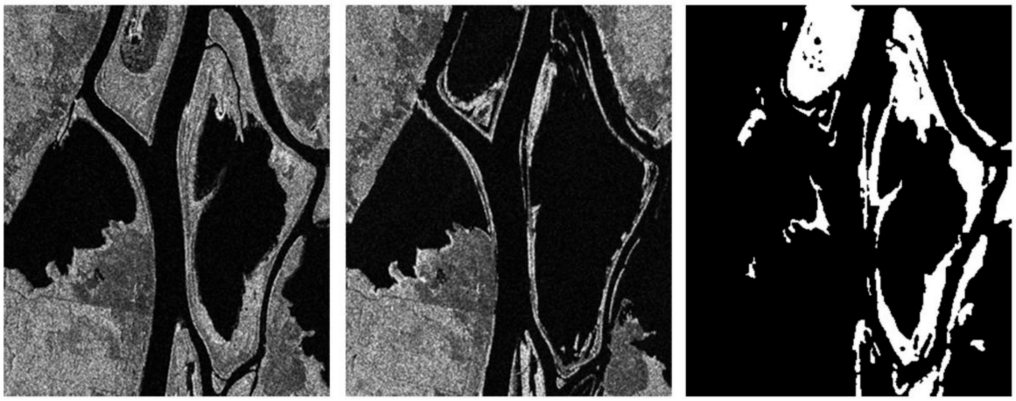

(**a**) (**b**) (**c**)

Figure 5. Ottawa data. (**a**) Image acquired in May 1997; (**b**) image acquired in August 1997; (**c**) ground-truth image.

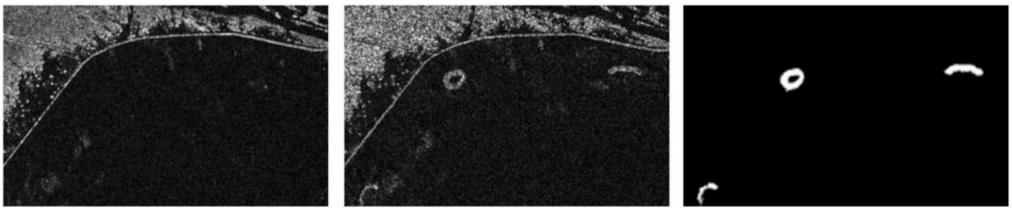

(**a**) (**b**) (**c**)

Figure 6. Coastline data. (**a**) Image acquired in June 2008; (**b**) image acquired in June 2009; (**c**) ground-truth image.

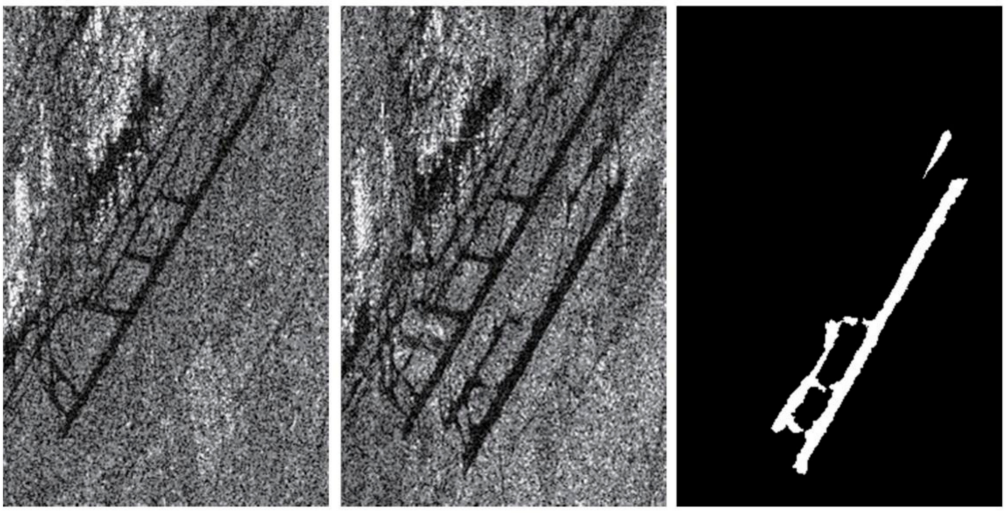

(**a**) (**b**) (**c**)

Figure 7. De Gaulle Airport data. (**a**) Image acquired in July 1997; (**b**) image acquired in October 1998; (**c**) ground-truth image.

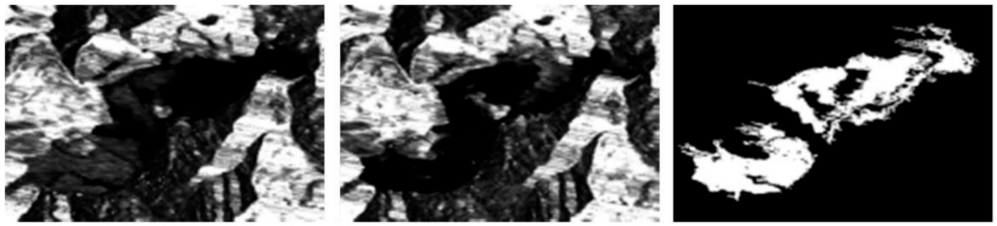

(**a**) (**b**) (**c**)

Figure 8. Wenchuan data. (**a**) Image acquired 3 March 2008; (**b**) image acquired 16 June 2008; (**c**) ground-truth image.

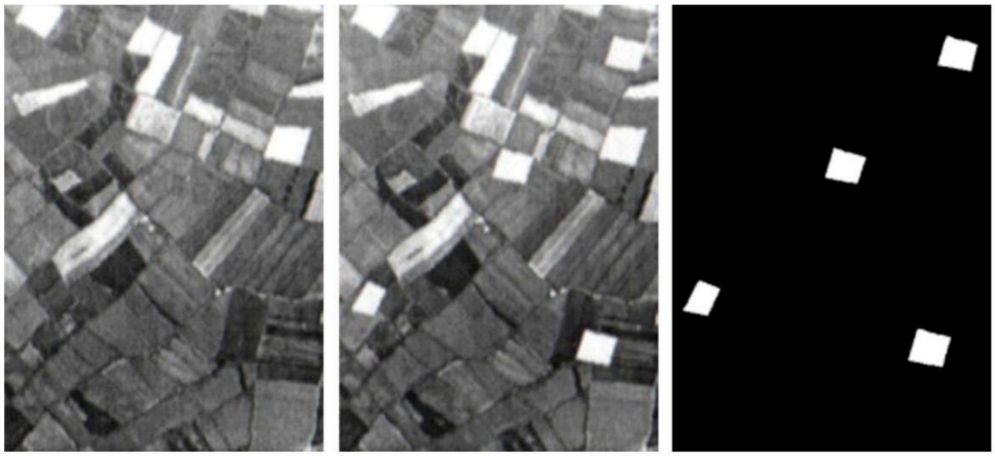

(**a**) (**b**) (**c**)

Figure 9. Simulated data. (**a**) Image acquired at Time 1; (**b**) image acquired at Time 2; (**c**) ground-truth image.

4.2. Experimental Settings

In this section, 10 closely related algorithms are compared: PCAKM [57], change detection using log-ratio and Otsu (LROtsu) [34], change detection using mean-ratio and Otsu (MROtsu) [34], change detection using log-ratio and FCM (LRFCM) [58], change detection utilizing Gabor wavelet and two-level clustering (GaborTLC) [59], LMT [60], PCANet [50], NRELM [55], change detection using neighborhood-based ratio and collaborative representation (NRCR) [61], convolutional-wavelet neural networks for change detection (CWNN) [53]. We used the relevant parameter values of the original articles proposed by the authors. In the proposed method, the parameter's value setting in the CWNN model is consistent with that in reference [53]. A total of 10,000 pixels were randomly selected from Ω_u and Ω_c as the real samples, and 10,000 virtual samples were generated based upon these real samples. Table 2 shows the parameter settings of different methods.

Table 2. The parameter settings of different methods.

Name/Reference	Parameter Settings
PCAKM [57]	$h = 4,\ S = 3$
LROtsu [34]	None
MROtsu [34]	None
LRFCM [58]	None
GaborTLC [59]	$U = 8,\ V = 5,\ k_{\max} = 2\pi,\ f = \sqrt{2}$
LMT [60]	The size of median filter is $3 * 3$
PCANet [50]	$\sigma = 1.20,$ stage number : $2,\ k = 5$
NRELM [55]	$\sigma = 1.20,$ neighborhood size : $3,\ k = 5$
NRCR [61]	neighborhood size: 3
CWNN [53]	patch size $\omega = 7$
Proposed	patch size $\omega = 7$

To help judge the results of the change detection, five objective indicators were used as measures, namely, false positives (FPs) [50,62], false negatives (FNs) [50,63], overall errors (OEs) [50,64], percentage correct classification (PCC) [50,65], and kappa coefficient (KC) [50,66]. In the binary ground-truth image, we calculated the actual number of pixels belonging to the unchanged class (Nu) and the changed class (Nc). FP depicts the number of pixels belonging to the unchanged class but are falsely classified as the changed class. FN shows the number of pixels belonging to the changed class but are falsely classified as the unchanged class. The OE is the sum of FP and FN, and it is defined as follows:

$$\mathrm{OE} = \mathrm{FP} + \mathrm{FN} \tag{9}$$

PCC is calculated by the following:

$$\mathrm{PCC} = \frac{Nu + Nc - \mathrm{FP} - \mathrm{FN}}{Nu + Nc} \times 100\% \tag{10}$$

KC is defined as follows:

$$\mathrm{KC} = \frac{\mathrm{PCC} - \mathrm{PRE}}{1 - \mathrm{PRE}} \tag{11}$$

where

$$\mathrm{PRE} = \frac{(Nc - \mathrm{FN} + \mathrm{FP}) \cdot Nc + (Nu - \mathrm{FP} + \mathrm{FN}) \cdot Nu}{(Nc + Nu) \cdot (Nc + Nu)} \tag{12}$$

The quantitative evaluations of the change results computed by the proposed and comparison algorithms are summarized in Tables 3–8.

4.3. Results and Discussions

The corresponding experimental results of the Ottawa data set are reported in Table 3 and Figure 10. In Figure 10, we notice that the change map obtained by the proposed method outperformed other algorithms, and yielded better local consistency and fewer isolated pixels. The change maps generated by LROtsu, MROtsu, and LRFCM had many error pixels, and the three algorithms had the worst capacity to suppress the noise. Therefore, the FP values of LROtsu, MROtsu, and LRFCM were relatively high, the values were twice the FP value obtained by the proposed algorithm, as shown in Table 3. The change maps computed by PCAKM, GaborTLC, and LMT missed some changed regions, but the detection of the unchanged area was more accurate. Therefore, the FN values of the corresponding three methods were higher, while the FP values were lower, which was consistent with the data shown in Table 3. The PCANet, NRELM, NRCR, and CWNN techniques missed some unchanged regions. The OE value of the proposed algorithm for the Ottawa data set was reduced by 521, 229, 949, and 285 over PCANet, NRELM, NRCR, and CWNN, respectively. The PCC value of the proposed technique was improved by 0.51, 0.22, 0.93, and 0.28% over PCANet, NRELM, NRCR, and CWNN, respectively. KC was a comprehensive evaluation index; the KC value of the proposed algorithm was improved by 1.97, 1.03, 3.36, and 1.10% over PCANet, NRELM, NRCR, and CWNN, respectively.

The simulation results for the Coastline data set are shown in Figure 11 and Table 4. From Figure 11, we see that the PCAKM, LROtsu, MROtsu, LRFCM, GaborTLC, and NRCR had many noise spots, and the visual effect of change detection was poor with large FP. The change map generated by LMT was an improvement compared to the previous algorithms, but it missed some changed regions with large FN. Compared to the PCANet, NRELM, and CWNN methods, the OE value of the proposed method for the Coastline data set was reduced by 13,920, 5819, and 13,330, respectively. The PCC value of the proposed algorithm was improved by 11.04, 4.62, and 10.58% over PCANet, NRELM, and CWNN, respectively. The KC value of the proposed method was improved by 69.53, 55.20, and 69.40% over PCANet, NRELM, and CWNN, respectively. From the analysis of the results for the Coastline data set, the change map computed by the proposed method had a better change detection effect.

Table 3. Quantitative measures of different methods for the Ottawa data set.

	FP	FN	OE	PCC(%)	KC(%)
PCAKM [57]	582	1901	2483	97.55	90.49
LROtsu [34]	2087	2741	4828	95.24	81.83
MROtsu [34]	2690	238	2928	97.12	89.80
LRFCM [58]	2106	2723	4829	95.24	81.85
GaborTLC [59]	253	2531	2784	97.26	89.07
LMT [60]	23	5266	5289	94.79	77.43
PCANet [50]	1087	985	2072	97.96	92.35
NRELM [55]	538	1242	1780	98.25	93.29
NRCR [61]	1723	777	2500	97.54	90.96
CWNN [53]	965	871	1836	98.19	93.22
Proposed	994	557	1551	98.47	94.32

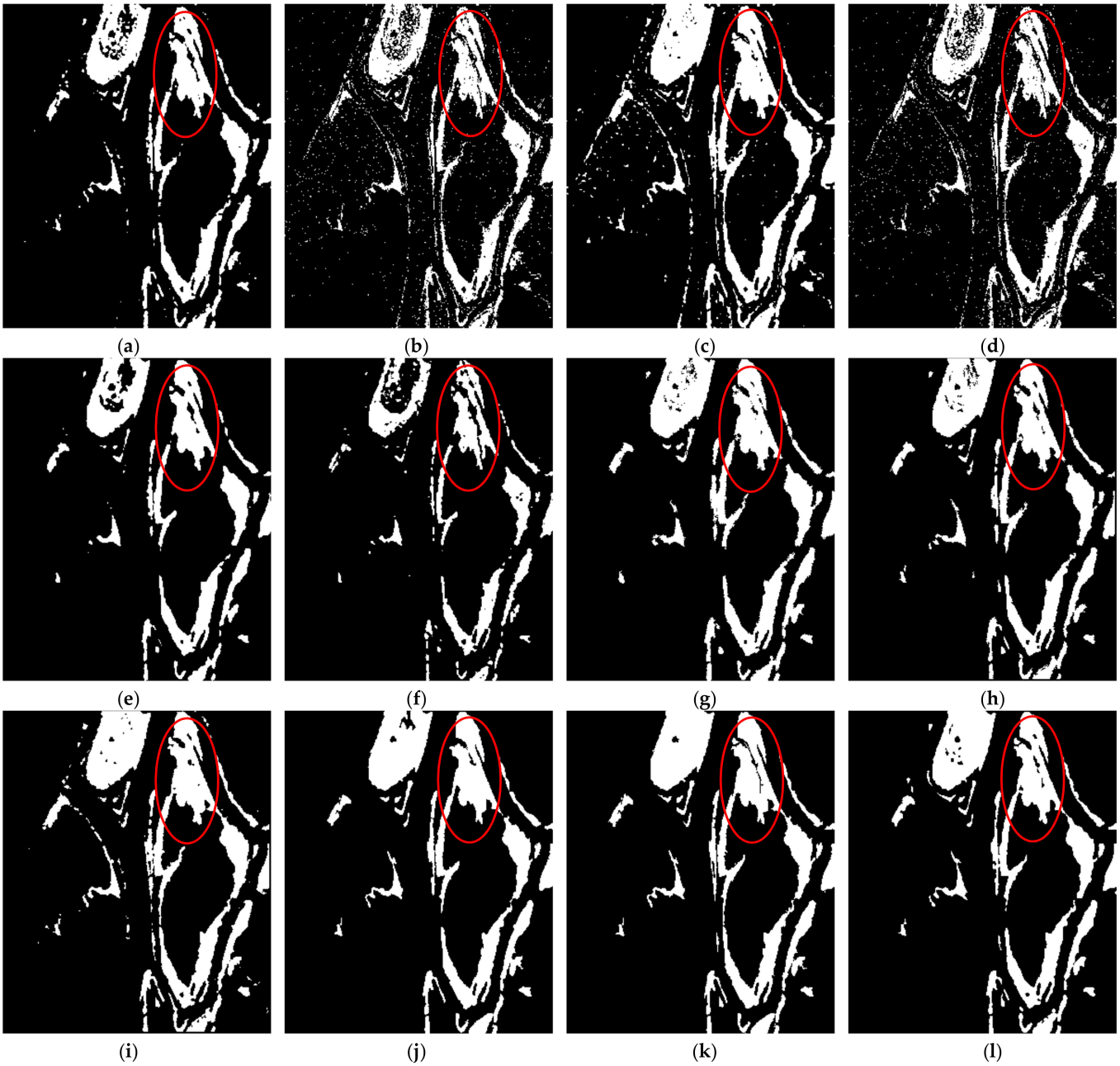

Figure 10. Change detection results of the Ottawa data set. (**a**) PCAKM; (**b**) LROtsu; (**c**) MROtsu; (**d**) LRFCM; (**e**) GaborTLC; (**f**) LMT; (**g**) PCANet; (**h**) NRELM; (**i**) NRCR; (**j**) CWNN; (**k**) Proposed; (**l**) Reference.

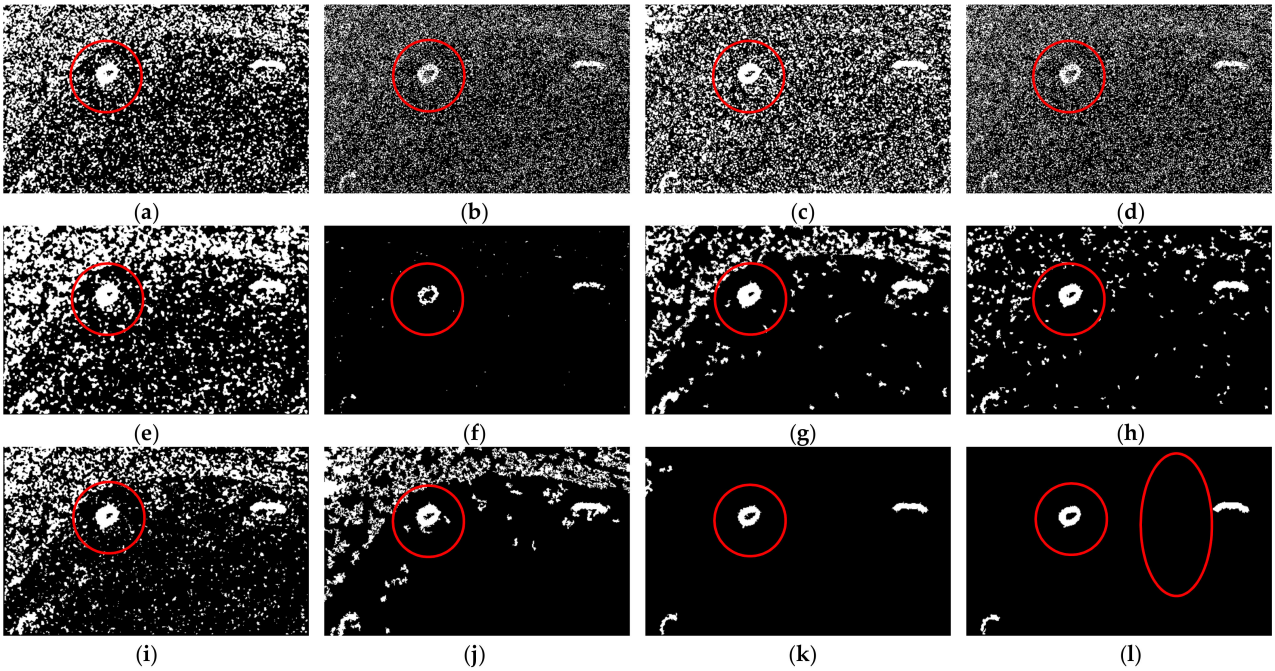

Figure 11. Change detection results of the Coastline dataset. (**a**) PCAKM; (**b**) LROtsu; (**c**) MROtsu; (**d**) LRFCM; (**e**) GaborTLC; (**f**) LMT; (**g**) PCANet; (**h**) NRELM; (**i**) NRCR; (**j**) CWNN; (**k**) Proposed; (**l**) Reference.

Table 4. Quantitative measures of different methods for the Coastline data set.

	FP	FN	OE	PCC(%)	KC(%)
PCAKM [57]	39,426	25	39,451	68.69	4.30
LROtsu [34]	30,059	280	30,339	75.92	4.62
MROtsu [34]	43,863	39	43,902	65.16	3.63
LRFCM [58]	32,488	254	32,742	74.01	4.30
GaborTLC [59]	36,359	6	36,365	71.14	4.91
LMT [60]	139	650	789	99.37	63.59
PCANet [50]	14,387	8	14,395	88.58	14.00
NRELM [55]	6271	23	6294	95.00	28.33
NRCR [61]	21,633	12	21,645	82.82	9.15
CWNN [53]	13,754	51	13,805	89.04	14.13
Proposed	348	127	475	99.62	83.53

The simulation results for the De Gaulle Airport data set are given in Figure 12 and Table 5. From Figure 12, we see that the PCAKM, LROtsu, MROtsu, and LRFCM methods yielded much noise with large FP. The change results computed by GaborTLC, PCANet, NRELM, NRCR, and CWNN were poor. The LMT missed more changed regions with the largest FN value. Compared with the change maps generated by other algorithms, our method had a better performance in change detection on the De Gaulle Airport data set. In Table 5, we can observe that the values of OE, PCC, and KC generated by the proposed method were the best. The PCC value computed by the proposed method was improved by 12.93, 7.36, 15.52, and 9.07% over PCANet, NRELM, NRCR, and CWNN, respectively. The KC value computed by the proposed method was improved by 39.15, 31.52, 43.26, and 33.52% over PCANet, NRELM, NRCR, and CWNN, respectively. This means that the detection accuracy of our algorithm performed on the De Gaulle Airport data set was the highest compared to other approaches.

The simulation results for the Wenchuan data set are given in Figure 13 and Table 6. In Figure 13, we see that LROtsu, MROtsu, and LRFCM generated poor change detection results with some noise points; these three methods detected more unchanged areas as changed, so the corresponding FP values were large. The change detection results computed by PCAKM, GaborTLC, LMT, and NRELM were similar, but the results were

still not ideal. In Table 6, we see that the proposed method had the least number of overall errors (OEs), and the values of PCC and KC were the best. The OE value of the proposed method for the Wenchuan data set was reduced by 1406, 3341, and 4900 over PCANet, NRCR, and CWNN, respectively. The PCC value of the proposed technique was improved by 1.05, 2.51, and 3.68% over PCANet, NRCR, and CWNN, respectively. The KC value of the proposed approach was improved by 4.82, 12.03, and 17.75% over PCANet, NRCR, and CWNN, respectively. The display of these data was obviously consistent with the analysis of the above image results. The change map generated by the proposed technique had higher detection accuracy and was closer to the reference true value image.

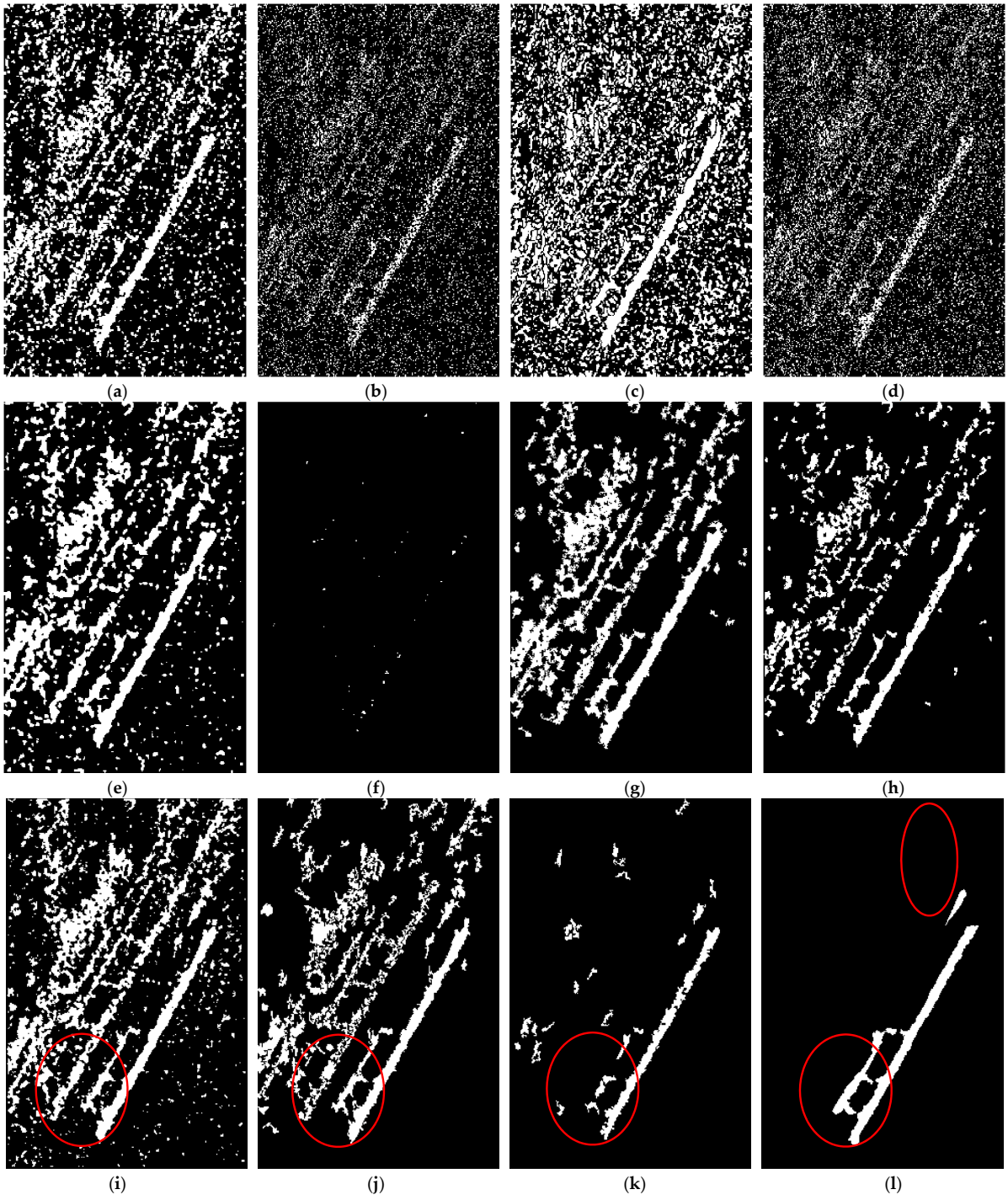

Figure 12. Change detection results of the De Gaulle Airport data set. (**a**) PCAKM; (**b**) LROtsu; (**c**) MROtsu; (**d**) LRFCM; (**e**) GaborTLC; (**f**) LMT; (**g**) PCANet; (**h**) NRELM; (**i**) NRCR; (**j**) CWNN; (**k**) Proposed; (**l**) Reference.

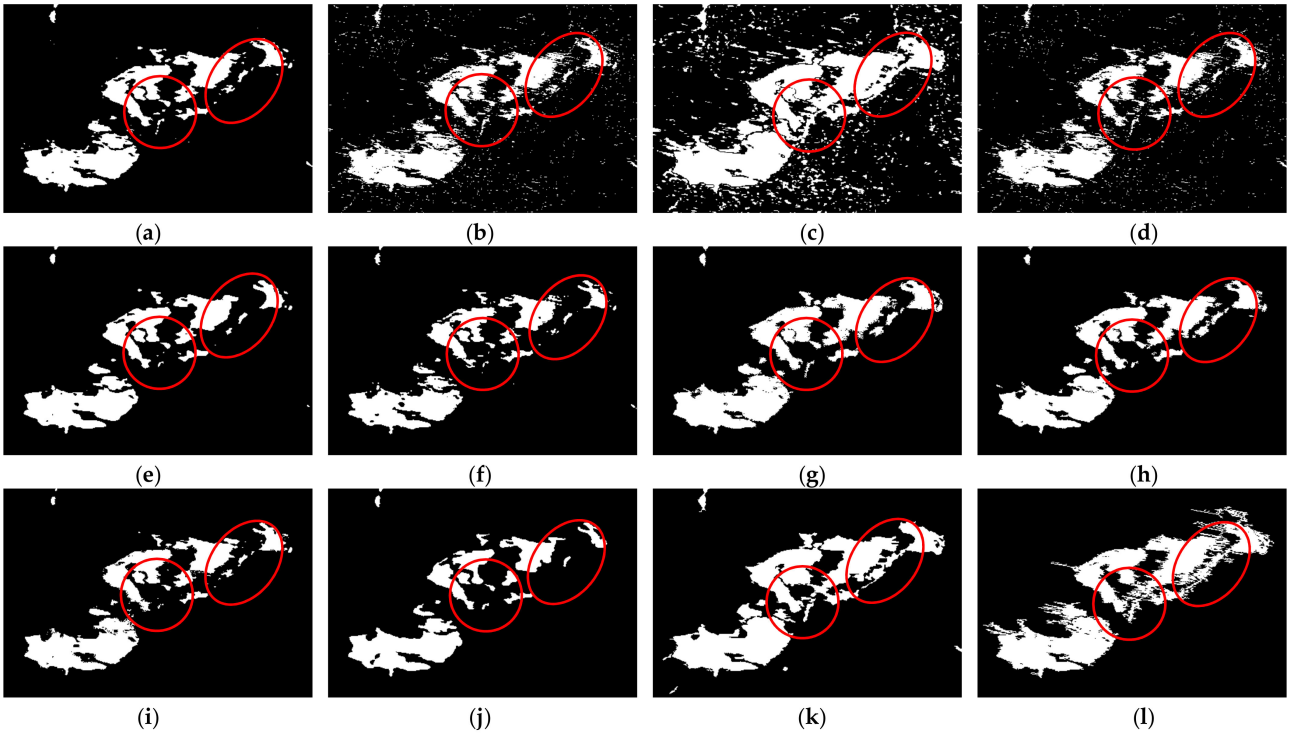

Figure 13. Change detection results of the Wenchuan data set. (**a**) PCAKM; (**b**) LROtsu; (**c**) MROtsu; (**d**) LRFCM; (**e**) GaborTLC; (**f**) LMT; (**g**) PCANet; (**h**) NRELM; (**i**) NRCR; (**j**) CWNN; (**k**) Proposed; (**l**) Reference.

Table 5. Quantitative measures of different methods for the De Gaulle Airport data set.

	FP	FN	OE	PCC(%)	KC(%)
PCAKM [57]	20,199	581	20,780	76.60	15.27
LROtsu [34]	11,446	1856	13,302	85.02	12.75
MROtsu [34]	29,189	441	29,630	66.63	10.15
LRFCM [58]	14,529	1644	16,173	81.79	11.60
GaborTLC [59]	17,051	436	17,487	80.31	19.59
LMT [60]	45	3248	3293	96.29	3.29
PCANet [50]	13,378	387	13,765	84.50	25.16
NRELM [55]	8060	761	8821	90.07	32.79
NRCR [61]	15,584	480	16,064	81.91	21.05
CWNN [53]	9794	541	10,335	88.36	30.79
Proposed	1156	1127	2283	97.43	64.31

Table 6. Quantitative measures of different methods for the Wenchuan data set.

	FP	FN	OE	PCC(%)	KC(%)
PCAKM [57]	939	7111	8050	93.95	76.27
LROtsu [34]	2574	6609	9183	93.10	74.00
MROtsu [34]	11,087	1723	12,810	90.37	70.95
LRFCM [58]	2527	6640	9167	93.11	74.01
GaborTLC [59]	689	8153	8842	93.35	73.27
LMT [60]	635	9333	9968	92.51	69.11
PCANet [50]	1366	5438	6804	94.89	80.73
NRELM [55]	988	6248	7236	94.56	79.04
NRCR [61]	582	8157	8739	93.43	73.52
CWNN [53]	578	9720	10,298	92.26	67.80
Proposed	2239	3159	5398	95.94	85.55

The simulation results for the simulated data set are shown in Table 7 and Figure 14. Some isolated noise points were generated by the PCAKM, LROtsu, MROtsu, LRFCM, and

LMT algorithms, and the FP values computed by the corresponding five methods were high. GaborTLC performed better than the previously mentioned change detection approaches. PCANet, NRELM, NRCR, and CWNN missed some changed regions with a large FN, although the four methods were effective for noise suppression. The proposed method effectively suppressed the noise and achieved a better detection effect that was closer to the true value image. The PCC value computed by the proposed method was improved by 0.83, 1.45, 0.79, and 1.24% over PCANet, NRELM, NRCR, and CWNN, respectively. The KC value generated by the proposed method was improved by 20.32, 41.38, 19.41, and 33.18% over PCANet, NRELM, NRCR, and CWNN, respectively.

To evaluate the superiority of the algorithm more accurately, we averaged the experimental data of five groups of SAR images, as shown in Table 8. Figure 15 shows the objective performance of different change detection algorithms on five SAR data sets. For each metric, the scores computed by an approach to different SAR data sets were connected to obtain a curve, and the average score is given in the legend, so we can directly see the fluctuation of data. In Table 8, we see that the values of OE, PCC, and KC computed by the proposed method were the best. Although the MROtsu method had the smallest miss detection rate, it had a higher false detection rate, and the values of FP and OE were the highest. LMT had the lowest false detection rate, but it had the highest miss detection rate, that is to say, the FN was the highest. In qualitative and quantitative analyses, our algorithm had absolute advantages in detection efficiency for SAR images.

Table 7. Quantitative measures of different methods for the simulated data set.

	FP	FN	OE	PCC(%)	KC(%)
PCAKM [57]	340	299	639	99.59	92.29
LROtsu [34]	857	244	1101	99.30	87.52
MROtsu [34]	4511	49	4560	97.10	63.42
LRFCM [58]	1327	184	1511	99.04	83.80
GaborTLC [59]	177	358	535	99.66	93.37
LMT [60]	1863	127	1990	98.74	79.87
PCANet [50]	27	1638	1665	98.94	75.22
NRELM [55]	25	2626	2651	98.32	54.16
NRCR [61]	10	1599	1609	98.98	76.13
CWNN [53]	45	2267	2312	98.53	62.36
Proposed	104	257	361	99.77	95.54

Table 8. The average quantitative measures of different methods for the five data sets.

	FP	FN	OE	PCC(%)	KC(%)
PCAKM [57]	12,297	1983	14,281	87.28	55.72
LROtsu [34]	9405	2346	11,751	89.72	52.14
MROtsu [34]	18,268	498	18,766	83.28	47.59
LRFCM [58]	10,595	2289	12,884	88.64	51.11
GaborTLC [59]	10,906	2297	13,203	88.34	56.04
LMT [60]	541	3725	4266	96.34	58.66
PCANet [50]	6049	1691	7740	92.97	57.49
NRELM [55]	3176	2180	5356	95.24	57.52
NRCR [61]	7906	2205	10,111	90.94	54.16
CWNN [53]	5027	2690	7717	93.28	53.66
Proposed	968	1045	2014	98.25	84.65

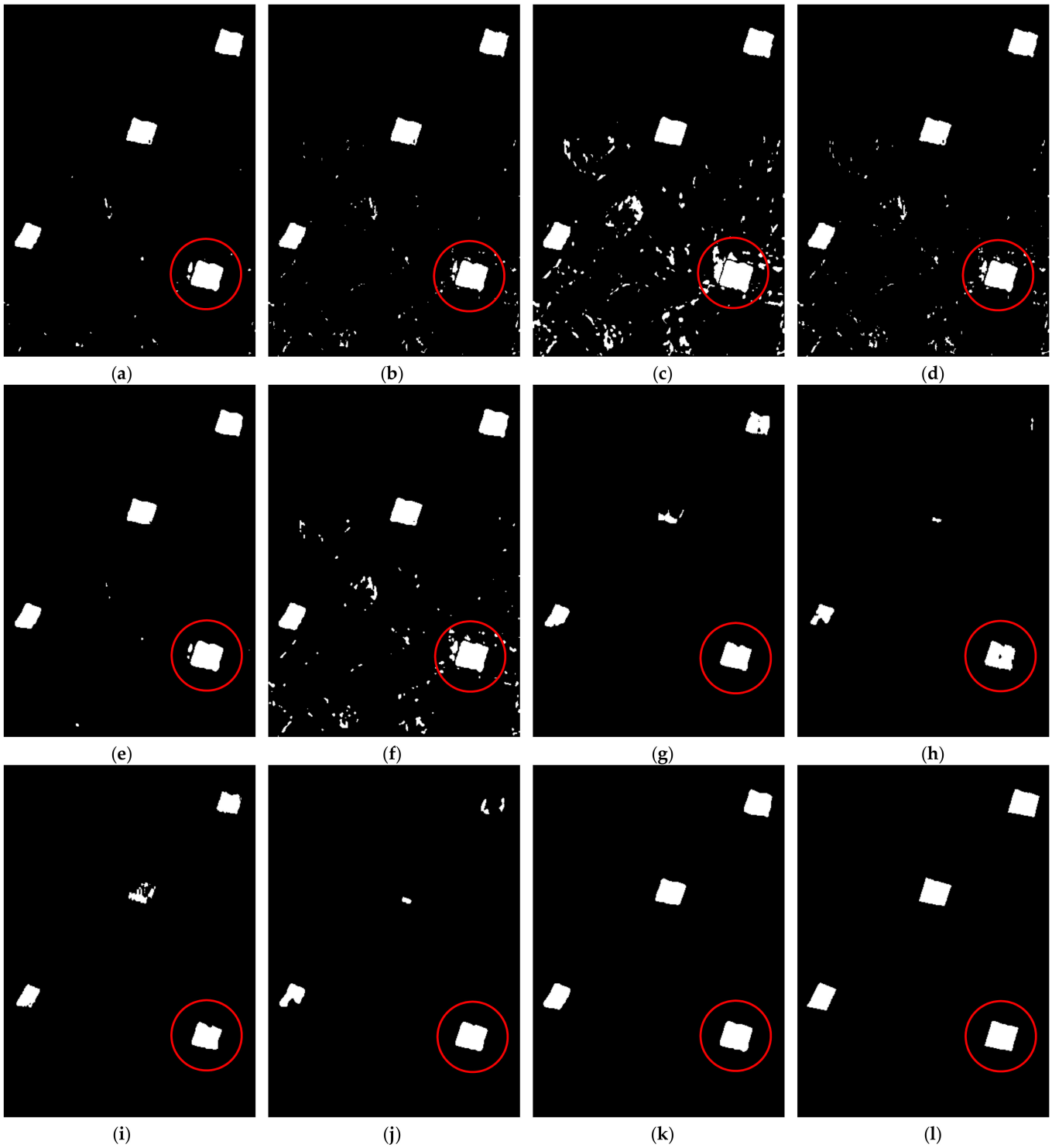

Figure 14. Change detection results of the simulated dataset. (**a**) PCAKM; (**b**) LROtsu; (**c**) MROtsu; (**d**) LRFCM; (**e**) GaborTLC; (**f**) LMT; (**g**) PCANet; (**h**) NRELM; (**i**) NRCR; (**j**) CWNN; (**k**) Proposed; (**l**) Reference.

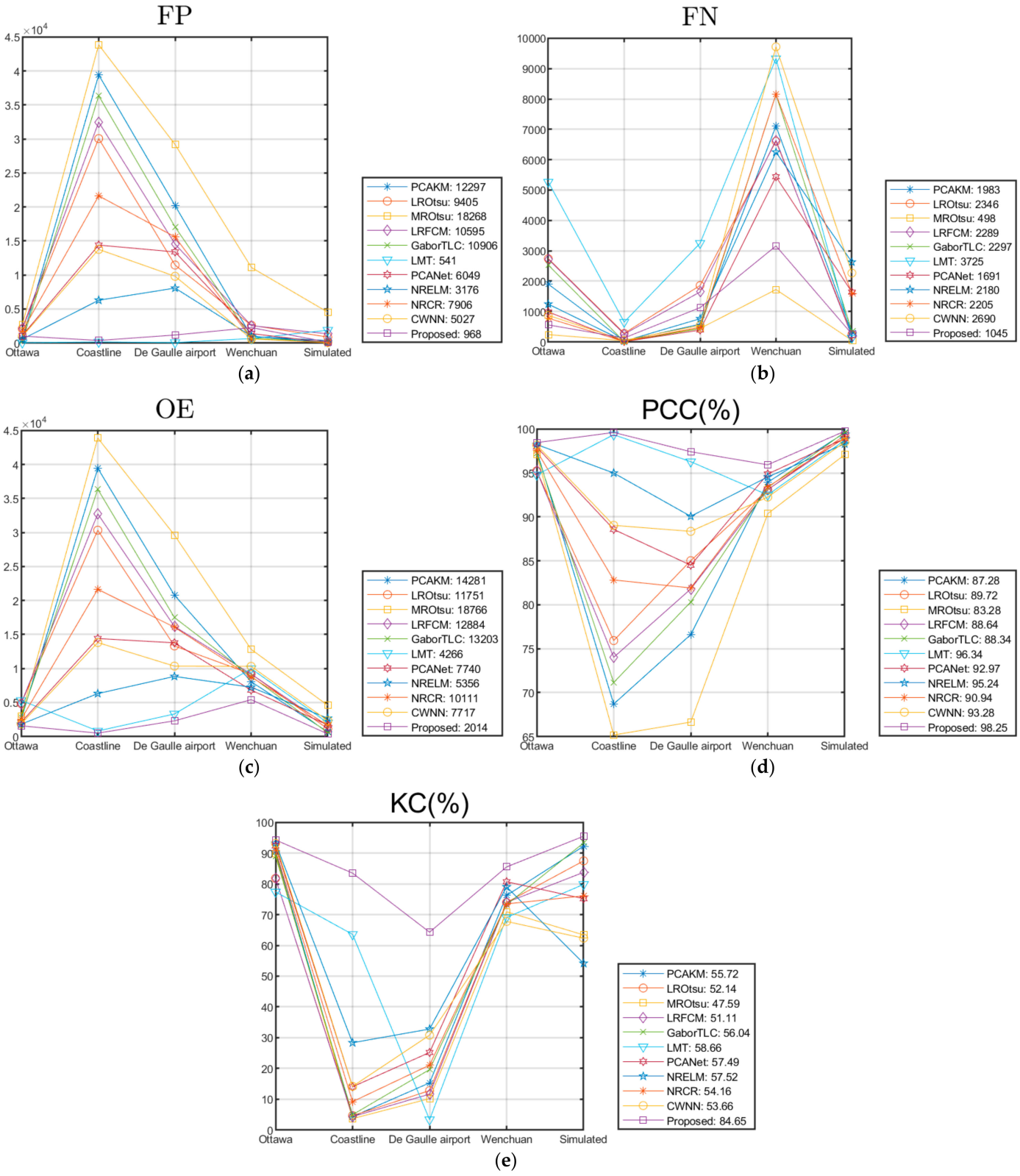

Figure 15. Objective performance of different change detection algorithms on five SAR data sets. (**a**) FP; (**b**) FN; (**c**) OE; (**d**) PCC; (**e**) KC.

5. Conclusions

In this paper, an effective SAR image change detection algorithm based on saliency-guided convolutional neural networks was proposed. The saliency map was adopted to guide the search for the interest regions in the initial difference image computed by a log-ratio operator, and the noise in the saliency map could be suppressed to some extent with the Otsu method. Then an enhanced difference image was generated by using the binarized saliency map and denoised input images. The hierarchical fuzzy c-means was used for pre-classification, and the final change map was obtained by the CWNN model. The experimental results demonstrated the effectiveness of the proposed change detection technique. Because the traditional saliency detection and the clustering model methods were used in the proposed algorithm, it was not an end-to-end deep learning model for SAR image change detection, so in future work, an end-to-end CWNN model for image change detection is what we need to construct.

Author Contributions: The experimental measurements and data collection were carried out by L.L. and H.M. The manuscript was written by L.L. with the assistance of H.M. and Z.J. All authors reviewed the manuscript. All authors have read and agreed to the published version of the manuscript.

Funding: This work was supported by the Shanghai Aerospace Science and Technology Innovation Fund under Grant No. SAST2019-048.

Institutional Review Board Statement: Not applicable.

Informed Consent Statement: Not applicable.

Data Availability Statement: Not applicable.

Conflicts of Interest: The authors declare no conflict of interest.

References

1. Chen, H.; Zhang, K.; Xiao, W. Building change detection in very high-resolution remote sensing image based on pseudo-orthorectification. *Int. J. Remote Sens.* **2021**, *42*, 2686–2705. [CrossRef]
2. Wang, C.; Wang, X. Building change detection from multi-source remote sensing images based on multi-feature fusion and extreme learning machine. *Int. J. Remote Sens.* **2021**, *42*, 2246–2257. [CrossRef]
3. Huo, J.-Y.; Mu, L. Fast change detection method for remote sensing image based on method of connected area labeling and spectral clustering algorithm. *J. Appl. Remote Sens.* **2021**, *15*, 016506. [CrossRef]
4. Zhao, J.; Liu, S.; Wan, J.; Yasir, M.; Li, H. Change detection method of high resolution remote sensing image based on DS evidence theory feature fusion. *IEEE Access* **2021**, *9*, 4673–4687. [CrossRef]
5. Dong, H.; Ma, W.; Jiao, L.; Liu, F.; Li, L. A multiscale self-attention deep clustering for change detection in SAR images. *IEEE Trans. Geosci. Remote Sens.* **2021**, 1–16. [CrossRef]
6. Jung, J.; Yun, S.H. Evaluation of coherent and incoherent landslide detection methods based on synthetic aperture radar for rapid response: A case study for the 2018 Hokkaido Landslides. *Remote Sens.* **2020**, *12*, 265. [CrossRef]
7. Yang, G.; Li, H.; Wang, W. Unsupervised change detection based on a unified framework for weighted collaborative representation with RDDL and fuzzy clustering. *IEEE Trans. Geosci. Remote Sens.* **2019**, *57*, 8890–8903. [CrossRef]
8. Deledalle, C.-A.; Denis, L.; Tupin, F. Iterative weighted maximum likelihood denoising with probabilistic patch-based weights. *IEEE Trans. Image Process.* **2009**, *18*, 2661–2672. [CrossRef]
9. Yu, Y.; Acton, S.T. Speckle reducing anisotropic diffusion. *IEEE Trans. Image Process.* **2002**, *11*, 1260–1270.
10. Farhadiani, R.; Homayouni, S.; Safari, A. Hybrid SAR speckle reduction using complex wavelet shrinkage and non-local PCA-based filtering. *IEEE J. Sel. Top. Appl. Earth Obs. Remote Sens.* **2019**, *12*, 1489–1496. [CrossRef]
11. Devapal, D.; Kumar, S.S.; Jojy, C. A novel approach of despeckling SAR images using nonlocal means filtering. *J. Indian Soc. Remote Sens.* **2016**, *45*, 443–450. [CrossRef]
12. Hu, T.; Li, W.; Liu, N.; Tao, R.; Zhang, F.; Scheunders, P. Hyperspectral Image restoration using adaptive anisotropy total variation and nuclear norms. *IEEE Trans. Geosci. Remote Sens.* **2021**, *59*, 1516–1533. [CrossRef]
13. Parrilli, S.; Poderico, M.; Angelino, C.V.; Verdoliva, L. A nonlocal SAR image denoising algorithm based on LLMMSE wavelet shrinkage. *IEEE Trans. Geosci. Remote Sens.* **2012**, *50*, 606–616. [CrossRef]
14. Zhou, Y.; Shi, J.; Yang, X.; Wang, C.; Kumar, D.; Wei, S.; Zhang, X. Deep multi-scale recurrent network for synthetic aperture radar images despeckling. *Remote Sens.* **2019**, *11*, 2462. [CrossRef]
15. Argenti, F.; Lapini, A.; Bianchi, T.; Alparone, L. A tutorial on speckle reduction in synthetic aperture radar images. *IEEE Geosci. Remote Sens. Mag.* **2013**, *1*, 6–35. [CrossRef]

16. Zheng, Y.; Zhang, X.; Hou, B.; Liu, G. Using combined difference image and *k*-means clustering for sar image change detection. *IEEE Geosci. Remote Sens. Lett.* **2014**, *11*, 691–695. [CrossRef]
17. Su, L.; Gong, M.; Sun, B. Change detection in synthetic aperture radar images based on non-local means with ratio similarity measurement. *Int. J. Remote Sens.* **2014**, *35*, 7673–7690. [CrossRef]
18. Lou, X.; Jia, Z.; Yang, J.; Kasabov, N. Change detection in SAR images based on the ROF model semi-implicit denoising method. *Sensors* **2019**, *19*, 1179. [CrossRef]
19. Wang, X.; Jia, Z.; Yang, J. Change detection in SAR images based on the logarithmic transformation and total variation de-noising method. *Remote Sens. Lett.* **2017**, *8*, 214–223. [CrossRef]
20. Liu, L.; Jia, Z.; Yang, J. SAR image change detection based on mathematical morphology and the k-means clustering algorithm. *IEEE Access* **2019**, *7*, 43970–43978. [CrossRef]
21. Zhang, Y.; Wang, C.; Ji, Y.; Chen, J.; Deng, Y.; Chen, J.; Jie, Y. Combining segmentation network and nonsubsampled contourlet transform for automatic marine raft aquaculture area extraction from sentinel-1 images. *Remote Sens.* **2020**, *12*, 4182. [CrossRef]
22. Li, L.; Ma, H.; Jia, Z.; Si, Y. A novel multiscale transform decomposition based multi-focus image fusion framework. *Multimed. Tools Appl.* **2021**, *80*, 12389–12409. [CrossRef]
23. Li, L.; Ma, H. Pulse coupled neural network-based multimodal medical image fusion via guided filtering and WSEML in NSCT domain. *Entropy* **2021**, *23*, 591. [CrossRef]
24. Kollem, S.; Reddy, K.; Rao, D. Improved partial differential equation-based total variation approach to non-subsampled con-tourlet transform for medical image denoising. *Multimed. Tools Appl.* **2021**, *80*, 2663–2689. [CrossRef]
25. Li, L.; Si, Y.; Wang, L. A novel approach for multi-focus image fusion based on SF-PAPCNN and ISML in NSST domain. *Multimed. Tools Appl.* **2020**, *79*, 24303–24328. [CrossRef]
26. Li, L.; Ma, H. Saliency-Guided nonsubsampled shearlet transform for multisource remote sensing image fusion. *Sensors* **2021**, *21*, 1756. [CrossRef] [PubMed]
27. Liu, Y.; Li, S.; Zhang, H. Multibaseline interferometric phase denoising based on kurtosis in the NSST domain. *Sensors* **2020**, *20*, 551. [CrossRef] [PubMed]
28. Chen, P.; Zhang, Y.; Jia, Z.; Yang, J.; Kasabov, N. Remote sensing image change detection based on nsct-hmt model and its application. *Sensors* **2017**, *17*, 1295. [CrossRef]
29. Li, S.; Fang, L.; Yin, H. Multitemporal image change detection using a detail-enhancing approach with nonsubsampled con-tourlet transform. *IEEE Geosci. Remote. Sens. Lett.* **2012**, *9*, 836–840.
30. Zhou, W.; Jia, Z.; Yu, Y. SAR image change detection based on equal weight image fusion and adaptive threshold in the NSST domain. *Eur. J. Remote. Sens.* **2018**, *51*, 785–794.
31. Shen, F.; Wang, Y.; Liu, C. Synthetic aperture radar image change detection based on Kalman filter and nonlocal means filter in the nonsubsampled shearlet transform domain. *J. Appl. Remote Sens.* **2020**, *14*, 016517. [CrossRef]
32. Hou, B.; Wei, Q.; Zheng, Y. Unsupervised change detection in SAR image based on Gauss-log ratio image fusion and com-pressed projection. *IEEE J. Sel. Top. Appl. Earth Obs. Remote Sens.* **2014**, *7*, 3297–3317. [CrossRef]
33. Zhang, Y.; Wang, S.; Wang, C.; Li, J.; Zhang, H. SAR image change detection using saliency extraction and shearlet transform. *IEEE J. Sel. Top. Appl. Earth Obs. Remote Sens.* **2018**, *11*, 4701–4710. [CrossRef]
34. Gong, M.; Zhou, Z.; Ma, J. Change detection in synthetic aperture radar images based on image fusion and fuzzy clustering. *IEEE Trans. Image Process.* **2011**, *21*, 2141–2151. [CrossRef] [PubMed]
35. Ma, J.; Gong, M.; Zhou, Z. Wavelet fusion on ratio images for change detection in SAR images. *IEEE Geosci. Remote Sens. Lett.* **2012**, *9*, 1122–1126. [CrossRef]
36. Geng, J.; Ma, X.; Zhou, X.; Wang, H. Saliency-Guided deep neural networks for SAR image change detection. *IEEE Trans. Geosci. Remote Sens.* **2019**, *57*, 7365–7377. [CrossRef]
37. Zheng, Y.; Jiao, L.; Liu, H.; Zhang, X.; Hou, B.; Wang, S. Unsupervised saliency-guided SAR image change detection. *Pattern Recognit.* **2017**, *61*, 309–326. [CrossRef]
38. Wang, X.; Gao, F.; Dong, J. Change detection for synthetic aperture radar images based on pattern and intensity distinctiveness analysis. In *Ninth International Conference on Graphic and Image Processing*; International Society for Optics and Photonics: Bellingham, WA, USA, 2018; Volume 10615, p. 1061548.
39. Majidi, M.; Ahmadi, S.; Shah-Hosseini, R. A saliency-guided neighbourhood ratio model for automatic change detection of SAR images. *Int. J. Remote Sens.* **2020**, *41*, 9606–9627. [CrossRef]
40. Li, M.; Li, M.; Zhang, P. SAR image change detection using PCANet guided by saliency detection. *IEEE Geosci. Remote Sens. Lett.* **2019**, *16*, 402–406. [CrossRef]
41. Moser, G.; Serpico, S. Generalized minimum-error thresholding for unsupervised change detection from SAR amplitude im-agery. *IEEE Trans. Geosci. Remote Sens.* **2006**, *44*, 2972–2982. [CrossRef]
42. Celik, T.; Ma, K.-K. Multitemporal image change detection using undecimated discrete wavelet transform and active contours. *IEEE Trans. Geosci. Remote Sens.* **2010**, *49*, 706–716. [CrossRef]
43. Hao, M.; Shi, W.; Deng, K.; Feng, Q. Superpixel-based active contour model for unsupervised change detection from satellite images. *Int. J. Remote Sens.* **2016**, *37*, 4276–4295. [CrossRef]
44. Jia, L.; Li, M.; Zhang, P.; Wu, Y.; Zhu, H. SAR Image change detection based on multiple kernel k-means clustering with local-neighborhood information. *IEEE Geosci. Remote Sens. Lett.* **2016**, *13*, 856–860. [CrossRef]

45. Shang, R.; Wen, A.; Liu, Y.; Jiao, L.; Stolkin, R. Synthetic aperture radar image change detection based on improved bilateral filtering and fuzzy C mean. *J. Appl. Remote Sens.* **2016**, *10*, 046017. [CrossRef]
46. Li, Z.; Jia, Z.; Liu, L.; Yang, J.; Kasabov, N. A method to improve the accuracy of SAR image change detection by using an image enhancement method. *ISPRS J. Photogramm. Remote Sens.* **2020**, *163*, 137–151. [CrossRef]
47. Zhang, X.; Liu, G.; Zhang, C.; Atkinson, P.M.; Tan, X.; Jian, X.; Zhou, X.; Li, Y. Two-Phase object-based deep learning for multi-temporal SAR image change detection. *Remote Sens.* **2020**, *12*, 548. [CrossRef]
48. Gao, Y.; Gao, F.; Dong, J.; Wang, S. Change detection from synthetic aperture radar images based on channel weighting-based deep cascade network. *IEEE J. Sel. Top. Appl. Earth Obs. Remote Sens.* **2019**, *12*, 4517–4529. [CrossRef]
49. Chan, T.-H.; Jia, K.; Gao, S.; Lu, J.; Zeng, Z.; Ma, Y. PCANet: A simple deep learning baseline for image classification? *IEEE Trans. Image Process.* **2015**, *24*, 5017–5032. [CrossRef] [PubMed]
50. Gao, F.; Dong, J.; Li, B.; Xu, Q. Automatic change detection in synthetic aperture radar images based on PCANet. *IEEE Geosci. Remote Sens. Lett.* **2016**, *13*, 1792–1796. [CrossRef]
51. Liu, T.; Li, Y.; Cao, Y.; Shen, Q. Change detection in multitemporal synthetic aperture radar images using dual-channel convolutional neural network. *J. Appl. Remote Sens.* **2017**, *11*, 1. [CrossRef]
52. Duan, Y.; Liu, F.; Jiao, L.; Zhao, P.; Zhang, L. SAR Image segmentation based on convolutional-wavelet neural network and markov random field. *Pattern Recognit.* **2017**, *64*, 255–267. [CrossRef]
53. Gao, F.; Wang, X.; Gao, Y.; Dong, J.; Wang, S. Sea ice change detection in sar images based on convolutional-wavelet neural networks. *IEEE Geosci. Remote Sens. Lett.* **2019**, *16*, 1240–1244. [CrossRef]
54. Ma, J.; Zhou, Z.; Wang, B. Infrared and visible image fusion based on visual saliency map and weighted least square optimi-zation. *Infrared Phys. Technol.* **2017**, *82*, 8–17. [CrossRef]
55. Gao, F.; Dong, J.; Li, B. Change detection from synthetic aperture radar images based on neighborhood-based ratio and ex-treme learning machine. *J. Appl. Remote. Sens.* **2016**, *10*, 046019. [CrossRef]
56. Goyal, A.; Meenpal, T. Patch-Based dual-tree complex wavelet transform for kinship recognition. *IEEE Trans. Image Process.* **2021**, *30*, 191–206. [CrossRef]
57. Celik, T. Unsupervised change detection in satellite images using principal component analysis and *k*-means clustering. *IEEE Geosci. Remote Sens. Lett.* **2009**, *6*, 772–776. [CrossRef]
58. Sharma, A.; Gulati, T. Change detection in remotely sensed images based on modified log ratio and fuzzy clustering. *Blockchain Technol. Innov. Bus. Process.* **2017**, *84*, 412–419. [CrossRef]
59. Li, H.-C.; Celik, T.; Longbotham, N.; Emery, W.J. Gabor Feature based unsupervised change detection of multitemporal SAR images based on two-level clustering. *IEEE Geosci. Remote Sens. Lett.* **2015**, *12*, 2458–2462. [CrossRef]
60. Sumaiya, M.N.; Kumari, R.S.S. Logarithmic mean-based thresholding for SAR image change detection. *IEEE Geosci. Remote Sens. Lett.* **2016**, *13*, 1726–1728. [CrossRef]
61. Gao, Y.; Gao, F.; Dong, J.; Wang, S. Sea ice change detection in SAR images based on collaborative representation. In Proceedings of the IGARSS 2018-2018 IEEE International Geoscience and Remote Sensing Symposium, Valencia, Spain, 22–27 July 2018; pp. 7320–7323.
62. He, Y.; Jia, Z.; Yang, J.; Kasabov, N. Multispectral image change detection based on single-band slow feature analysis. *Remote Sens.* **2021**, *13*, 2969. [CrossRef]
63. Yang, L.; Chen, Y.; Song, S.; Li, F.; Huang, G. Deep Siamese networks based change detection with remote sensing images. *Remote Sens.* **2021**, *13*, 3394. [CrossRef]
64. Shao, P.; Shi, W.; Liu, Z.; Dong, T. Unsupervised change detection using fuzzy topology-based majority voting. *Remote Sens.* **2021**, *13*, 3171. [CrossRef]
65. Wu, T.; Luo, J.; Fang, J.; Ma, J.; Song, X. Unsupervised object-based change detection via a weibull mixture model-based binarization for high-resolution remote sensing images. *IEEE Geosci. Remote Sens. Lett.* **2018**, *15*, 63–67. [CrossRef]
66. Wu, T.; Luo, J.; Zhou, Y.; Wang, C.; Xi, J.; Fang, J. Geo-object-based land cover map update for high-spatial-resolution remote sensing images via change detection and label transfer. *Remote Sens.* **2020**, *12*, 174. [CrossRef]